Atomic-Resolution Spectroscopic Imaging of Ensembles of Nanocatalyst Particles Across the Life of a Fuel Cell

Huolin L. Xin,[†,¶] Julia A. Mundy,[‡,¶] Zhongyi Liu,[*,§] Randi Cabezas,[∥] Robert Hovden,[‡] Lena Fitting Kourkoutis,[‡] Junliang Zhang,[§] Nalini P. Subramanian,[§] Rohit Makharia,[§] Frederick T. Wagner,[§] and David A. Muller[*,‡,⊥]

[†]Department of Physics and [‡]School of Applied and Engineering Physics, Cornell University, Ithaca, New York 14853, United States
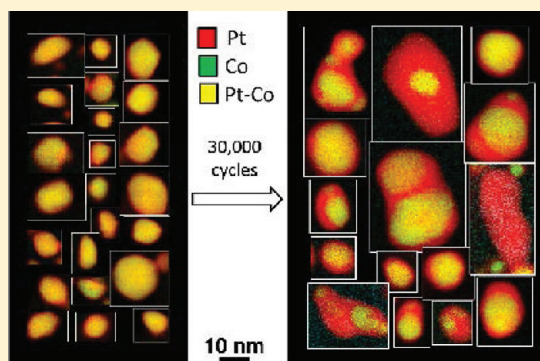[§]Electrochemical Energy Research Laboratory, General Motors, Honeoye Falls, New York 14472, United States
[∥]Electrical and Computer Engineering, Florida International University, Miami, Florida 33174, United States
[⊥]Kavli Institute at Cornell for Nanoscale Science, Ithaca, New York 14853, United States

Ⓢ Supporting Information

ABSTRACT: The thousand-fold increase in data-collection speed enabled by aberration-corrected optics allows us to overcome an electron microscopy paradox: how to obtain atomic-resolution chemical structure in individual nanoparticles yet record a statistically significant sample from an inhomogeneous population. This allowed us to map hundreds of Pt−Co nanoparticles to show atomic-scale elemental distributions across different stages of the catalyst aging in a proton-exchange-membrane fuel cell, and relate Pt−shell thickness to treatment, particle size, surface orientation, and ordering.

Bulk and reciprocal space measurements provide accurate ensemble averages of nanoparticle systems, yet in doing so lose the connections between microscopic degrees of freedom when integrating over the myriad of different particles in any representative sample. Out of necessity, nanoscale chemical imaging to date has relied on a handful of spectra collected from a few selected particles, as it often takes a few hours to record a spectral map of a single nanoparticle. However, nanoparticle systems—especially during electrocatalysis—are heterogeneous and have multiple competing processes running in parallel. Thus, identifying and quantifying dominant mechanisms requires statistics on scores to hundreds of particles in order to reliably connect the microstructure to the bulk properties. With the development of aberration-corrected scanning transmission electron microscopy (STEM)[1,2] and efficient electron energy loss spectra (EELS) collection systems, elemental concentrations and chemical bonding information can now be collected roughly a thousand times faster than on a conventional microscope, allowing rapid and reliable two-dimensional (2D) mapping of chemical distributions at atomic resolution.[3] While much of the focus of aberration correction has been on producing increasingly small sub-angstrom electron beams, here we instead stop at an atomic-sized beam and increase the usable beam current. This

enabled us to collect over one million EELS spectra and map out the concentrations of all atomic species in hundreds of Pt−Co nanoparticles used as fuel cell electrocatalysts. We can thus quantify and correlate internal ordering, facet termination, and surface structure—nanoparticle by nanoparticle—to identify the dominant degradation chemistries that limit the catalyst's efficiency. These measurements would have taken years to record, and thus be too slow to provide feedback in a rapidly evolving field, were now collected in sessions of a few hours to days.

Addressing the degradation mechanisms in Pt−Co nanoparticles is a key step in the development of proton-exchange-membrane fuel cells (PEMFCs), one of the most promising alternatives to fossil fuel-based internal combustion engines; PEMFCs produce electricity with water as the only by-product.[4−6] The commercialization of PEMFCs is hindered by the sluggish cathodic oxygen reduction reaction (ORR, $H_2 + 1/2 O_2 = H_2O$) despite the use of precious metal Pt catalysts. To overcome the cost barrier, Pt alloys (Pt−M, where M represents transition metals[7−12] or rare earths[13]) are generally used to reduce the Pt loading in the cathode. Some of the Pt-

based alloy nanoparticles, such as the technologically relevant Pt–Co,[5] show enhanced ORR activity at the beginning of the fuel cell lifetime; however, they are not yet stable enough to maintain their advantage over pure Pt nanocatalysts by the end of their targeted life times.[5,14−18] This degradation during fuel cell operation is attributed to dissolution of material from the catalyst particles leading to mass loss;[19−21] corrosion and collapse of the carbon support leading to particle agglomeration;[19,22] a reduction in surface area for the remaining material as the average particle size increases; and a reduction in the specific activity from the remaining surface area as the particle composition and structure are altered.[18,23] While the first two issues are better understood and common to both Pt and Pt–M alloys, our focus here is on the final two issues that are determined by the less-well understood microscopic underpinnings and interplay between particle growth, surface chemistry, and catalytic activity.

Understanding the coarsening of these nanocatalysts, which leads to the decline in specific activity during operations, is essential; for the Pt–Co nanoparticles studied here, the specific activity of the alloyed particles drops to that of pure Pt by the end of the DOE targeted lifetime (Supporting Information Table S1 and S2). Two competing schools of thought have been proposed: Ostwald ripening by the transport of individual atoms[24,25] or coalescence by movement and collisions of whole nanoparticles.[26,27] To understand the relative importance of each mechanism for our system, we characterized the commercial Pt$_3$Co electrocatalyst (see Methods in Supporting Information) before and after voltage cycling in an operational fuel cell to establish a microstructure/catalytic activity relationship throughout the fuel cell lifecycle. We find that not only are both Ostwald ripening and coalescence statistically significant contributors in our material, but that there is a synergistic interplay between the two, as Pt redeposition is enhanced around coalesced particles compared to uncoalesced particles. A surprising consequence of the interplay is the suggestion that decreasing coalescence (by changing the support material for instance) might reduce the Ostwald ripening of the very thick Pt shells correlated with the loss in specific activity.

In addition, we also investigated precycled particles following a heat treatment to restore equilibrium structures and internal ordering to make contact with existing studies. This allowed us to compare our spatially resolved experiments on nanoparticles to macroscopically averaged single-crystal experiments and ab initio theories of equilibrium surface structure in vacuum. It also illustrates the difference between the ideal structures predicted for thermodynamically stable surfaces in vacuum and the actual structure after exposure to liquids. We identified monolayer segregation of Pt on the {111} facets of annealed nanoparticles, consistent with previously reported vacuum-annealed bulk {111} crystal surfaces,[11] however we also found no statistically significant Pt segregation was found on the {100} facets of the same nanoparticles in the ensemble, something that had not been possible to examine by bulk methods, although it is expected from Monte Carlo simulations.[11] This provides a useful check of the precision and sensitivity of our real-space sampling.

We then perform an acid leaching of these equilibrium particles to distill the impact of the acidic environment of the cathode from the effects of voltage cycling. This allows us to distinguish the chemistry from the electrochemistry when directly comparing samples at the beginning and end of fuel cell lifetime. After exposure to acid, a three-monolayer Pt shell

formed, surprisingly independent of crystal facet. The thickness of the shell indicates that the catalytic enhancement of acid leached Pt–Co nanoparticles over pure Pt cannot be due to a nearest neighbor electronic effect.[28,29]

It is important to note that considerable previous effort has been invested in determining the atomic distributions of Pt and Co within individual nanoparticles using annular dark-field (ADF) STEM.[14,23] The ADF-STEM imaging technique with its strong mass–thickness sensitivity (a function of the number of atoms viewed in projection, and their atomic numbers) can rapidly screen many particles.[30,31] While this works well for detecting heavy atoms in matrices of light atoms,[31−33] the converse is often not the case. For example, while the emergence of a Pt-rich shell surrounding a Pt$_3$Co core is expected as Co is soluble in acid whereas Pt is not,[11] it is difficult to distinguish between Co atoms and Co vacancies near the surface against a Pt background solely with ADF images. Similarly, it would be difficult to distinguish between Co-rich regions and voids in a dealloyed Pt/transition metal composite nanoparticle. The elastic-scattering cross section of Pt is 6–7 times that of Co and thus the electrons scattered by Pt dominate the signal. For Pt$_3$Co, only 2–6 of the projected 10–25 atoms in an atomic column of a 2–6 nm particle are Co; thus the contrast changes between stoichiometric Pt$_3$Co and pure Pt are less than the scattering from a single Pt atom or vacancy on the surface. This ambiguity was resolved with EELS of the inelastically scattered electrons. In particular, we used an EELS-optimized, 100 kV, fifth-order aberration-corrected Nion STEM[3] with a 1−1.4 Å diameter electron beam to determine the Pt and Co elemental distributions independently and unambiguously from their unique core-level binding energies with submonolayer resolution (see Methods in Supporting Information). The key advances here are correcting probe aberrations to fifth instead of third order, correcting key third-order aberrations at the entrance to the spectrometer to increase the collection angle from 25 to 90 mrad, using a high-brightness cold field emission source and trading source size for increased beam current.[3,34]

While EELS spectroscopic imaging allows for a direct measurement of the Pt and Co distributions in a nanoparticle, the size of a spectroscopic data set with a 1340-channel spectrum at each pixel limited the number of pixels in each image. This forced us to image each nanoparticle sequentially, rather than simultaneously acquiring a large number of particles, as can be done for ADF images, which at 1 channel/pixel use 1340 times less memory. To avoid any sampling bias in selecting which particles to map in EELS, we also recorded a large-area ADF image to determine the particle size distribution for all 946 nanoparticles (Supporting Information Figure S1) in the field of view. We then randomly selected a subset of roughly 1 in every 10 nanoparticles. Because of the larger variance in the tails of the particle-size distribution and almost uniform distribution of smaller particles (<5 nm radius in ADF), we deliberately oversampled larger particles (>5 nm radius) in the 30 000 voltage-cycled sample to obtain better counting statistics relating to the coarsening mechanism. Our EELS measurements were then weighted by the population distribution (Supporting Information Figure S2) such that we were not biased by sampling preferences; this ensures an accurate correspondence between our EELS results and the bulk electrochemical properties.

Figure 1 shows typical EELS spectroscopic images and outlines the consequences of the different processing pathways.
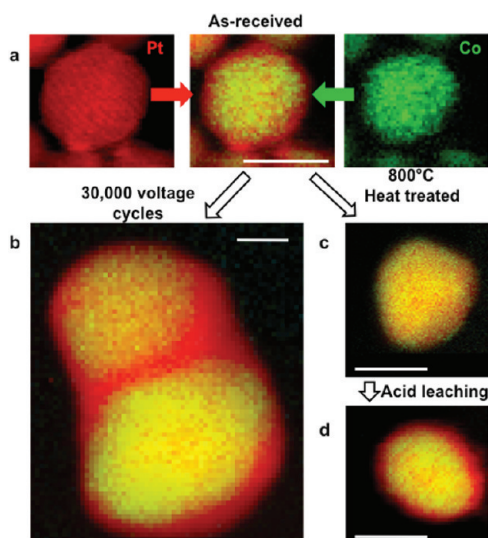
Figure 1. Typical EELS spectroscopic images of Pt–Co nanoparticles for the chemical and electrochemical processes studied here. The relative Pt concentration is shown in red and the Co concentration in green, so yellow indicates a Pt–Co alloy. The stripes in the Pt image of (a) are {111} lattice planes viewed at a slight mistilt. (a) As-received, showing 0.6 nm Co-free shell, (b) after 30K voltage-cycles, showing a coalescence of 2 smaller Pt–Co nanoparticles surrounded by a Co-free shell ~2–3 nm thick, (c) after heat-treatment of the as-received material, leading to a uniform Co distribution and no Co-free shell and (d) after acid-leaching the heat-treated sample, where a Co-free shell similar to that of the starting material (a) has returned. The scale bar for each image is 5 nm.

Core–shell structures with pure Pt shells and Pt–Co alloy cores were observed in the precycled "as-received" (Figure 1a), heat plus acid-treated (Figure 1d), and voltage-cycled (Figure 1b) samples. A relatively uniform elemental distribution throughout the particle interior was observed from the heat-treated sample (Figure 1c). As a resolution test in Figure 2a, the atomic-resolution EELS maps show Pt and Co ordering in a heat-treated Ll_2 Pt–Co nanoparticle, as does the accompanying ADF lattice image, although not all particles are ordered (Supporting Information Figure S4). The presence of a surface Pt monolayer on some facets was observed in the heat-treated sample, as seen in Figure 2b (atomic-resolution images) and Figure 3 (statistical analysis). In Figure 2b, a {111}-terminated facet of a heat-treated Pt–Co nanoparticle shows the surface structure predicted by Stamenkovic and co-workers for the equilibrium structure in vacuum;[11] the surface atomic layer is Pt (bright in the ADF image) and second plane from the surface is Co rich (dark in the ADF image indicating Co enrichment or Pt vacancies). The accompanying EELS line profile resolves the ambiguity, showing the reduced intensity in the second plane is from preferential Co-segregation, not Pt-vacancies.

However, a unique strength of this technique is that it enables the mapping of the Pt shell for an ensemble of particles from which we can construct a statistically significant facet-by-facet analysis rather than relying on the single analysis in Figure 2b. Figure 3 shows the effect of the acid leaching from a statistical comparison of the Pt shell thickness between the heat-treated and heat plus acid-treated samples (see Supporting Information Figure S11 for the spectroscopic maps of the particles). Histograms are shown for {111}, {100}, and all nanoparticle facets (including a handful of what may be {110} facets and facets that could not be indexed because the particles
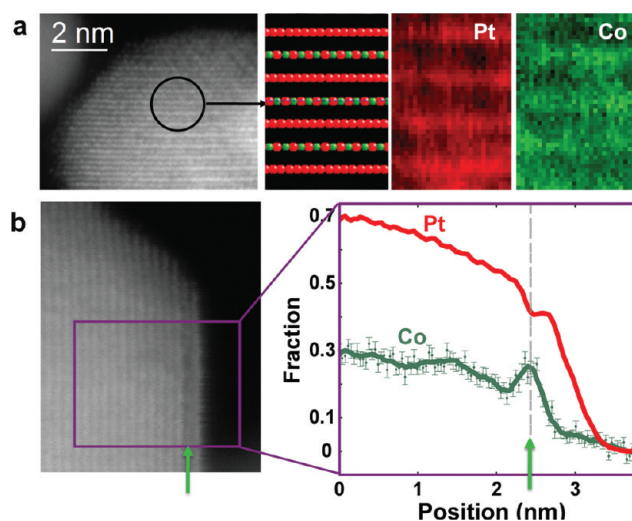

Figure 2. Atomic-resolution spectroscopic images of Pt–Co nanoparticles from the heat-treated sample. (a) A Ll_2 ordered Pt–Co nanoparticle with (001) planes oriented parallel to the electron beam. The Pt and Co maps show the alternating planes of the Pt and Pt/Co as shown in the model structure (Pt, red; Co, green). (b) A {111}-facet terminated Pt–Co nanoparticle, and the Pt/Co concentration profile across the facet showing a strong dealloying effect at the last two planes with the Co segregating to one layer below the surface, and Pt segregating to outermost plane. The Pt and Co signals are scaled to their nominal bulk compositions at $x = 0$.
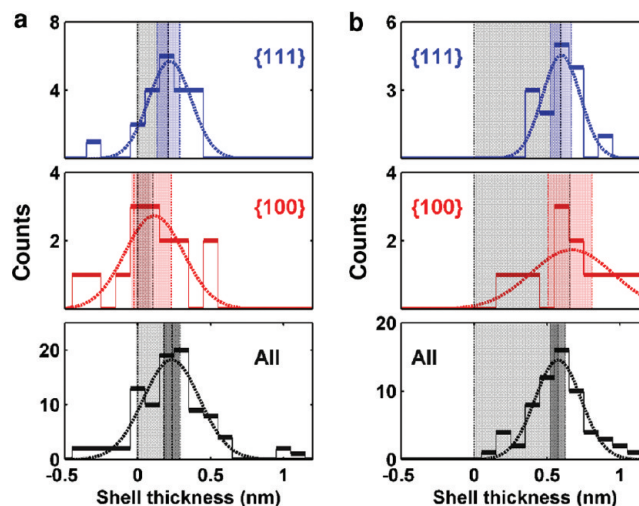

Figure 3. Histograms of the Pt shell thickness, measured from different facets of individual nanoparticles in (a) the heat-treated sample and (b) the acid-leached sample. The left and right boundary of the colored shaded area marks the two standard errors of the mean (95.4% confidence interval) and the right boundary of the gray shaded area marks the average shell thickness. The overlap of the red and gray areas for the {100} facets of the heat-treated sample shows that there is no statistically significant shell thickness there, whereas there is a 1.6 ± 0.5 Å (~1 monolayer) Pt shell on {111} heat-treated facets. In contrast, after acid treatment (b) the shell thickness has grown to 5.7 ± 0.3 Å (~2.5 monolayers) and is independent of facet orientation. For the heat-treated sample, of the 94 facets measured 21 could be indexed as {111} and 15 as {100}, while for the acid-leached material, of the 63 facets 15 were identified as {111} and 12 as {100}.

were not on axis; here "{100}" includes both the {100} of the $L1_2$ ordered structure and the {200} of the disordered structure). For the equilibrium heat-treated sample (Figure
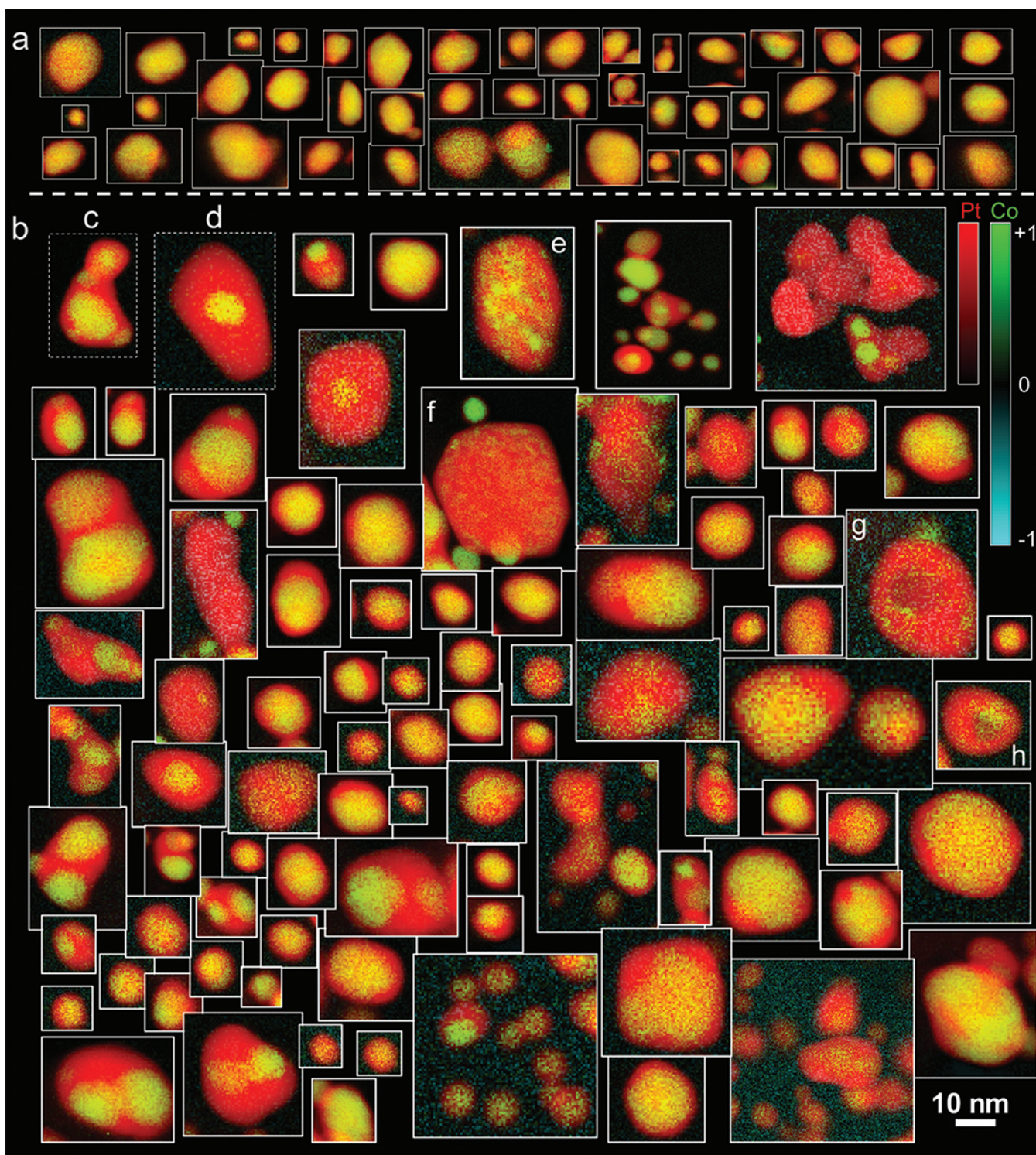
Figure 4. Collage of EELS spectroscopic images from the (a) as-received and (b) the voltage-cycled sample. As shown in the color bars, the relative Pt concentration, normalized in each separate image, is plotted in red and the Co concentration ranging from green to turquoise. Particles (c–h) from the cycled sample are discussed in more detail in the text. The selection of images shown is meant to display the diversity of particle types, not the statistical distribution of the types, which is covered in Figure 5.

3a), the Pt shell thickness on the {111} facets was 1.6 ± 0.5 Å (~1 monolayer) while that on the {100} was 0.6 ± 0.7 Å, a null result for segregation on {100} (two standard error of the mean, 95.4% confidence interval). This preferential segregation of one monolayer of Pt on the {111} planes agrees with studies of bulk surfaces as well as Monte Carlo simulations[11,35] and ADF image analysis of selected Pt₃Co nanoparticles.[14,23] We

are not aware of previous segregation studies on the {100} surface, although electrochemically the activities on the {100} and {111} Pt₃Ni surfaces are very different.[36] However, we next probe the integrity of this segregated layer in an aggressive oxidizing acidic environment, which provides an accelerated proxy to mimic the chemical environment of the cathode.
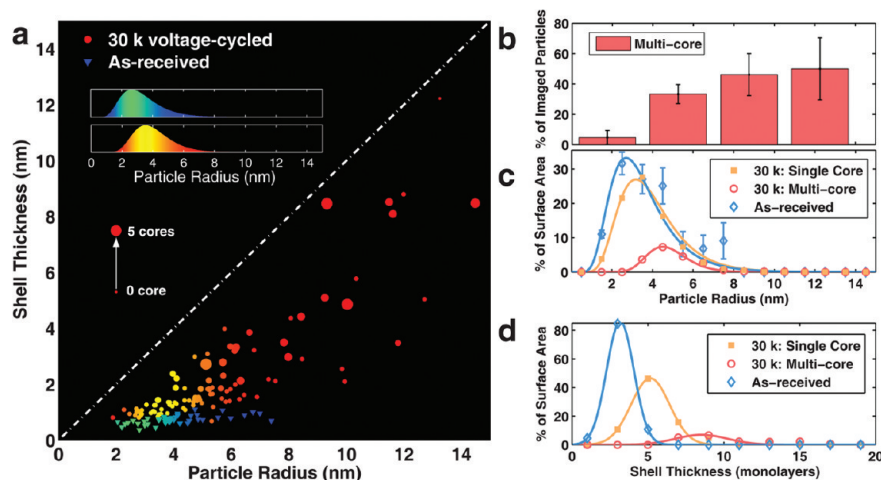
Figure 5. Statistical analyses of core−shell distributions of the Pt−Co nanoparticles from Figure 4. The particle populations, both before and after cycling in the fuel cell, follow log-normal distributions (Supplementary Figure S1). The colorbars in panel (a) relate the color of the markers to the surface-area-normalized probability of a spectroscopically measured particle's occurrence in an unbiased measurement. The Pt-rich, Co-free shell for the starting distribution of particles is almost independent of particle radius (measured by the effective Pt radius as shown in Supporting Information Figure S10). After cycling, there is a widespread in effective shell thickness, which increases as the particle size increases. The size of the marker depicts the number of distinct Co cores found in the particle with larger markers signifying more cores. The dashed white line marks where the Pt-shell would extend throughout the particle, that is, a total absence of Co. The fraction of measured particles that contain multiple Pt−Co cores (b) increases with particle size, accounting for roughly half the particles with radii larger than 6 nm. However, there are many more small particles than large, so surface area is dominated by the smaller particles (c). For understanding the impact of shell thickness on electrochemical activity, the fraction of surface area as a function of Pt-shell thickness is plotted in (d). After 30 000 voltage cycles (30K), the Pt-shell thickness has grown and is thicker for the multicore particles than the single core. The data presented in (c) and (d) were normalized to the population distribution (see Methods and Figure S2 in Supporting Information) such that we were not biased by sampling preferences.

Treatment of the thermally equilibrated particles in an oxidizing acid medium forms a 5.7 ± 0.3 Å (∼2.6 monolayers) thick Pt shell (Figure 3b). Unlike the equilibrium sample, the heat plus acid-treated sample exhibited a uniform Pt shell thickness on all facets, that is, there was no statistically significant difference in the Pt shell thickness on differently oriented facets. Thus it appears that the preference for a Pt skin on the {111} facets of the equilibrium particles does not survive in the cathode environment. This was unexpected because the density of surface sites is different for the different facets, suggesting leaching rates might be expected to be different as well. Possible explanations might be that either diffusion rates along different zone axes counteract this trend or the leaching occurs through a disordered intermediate. The particles also take on a more rounded appearance as the {111} facets that dominated the thermally annealed particles shrink to become comparable in area to the other facets.

The uniform Pt-shell thickness was also independent of particle size (Supporting Information Figure S3). This statistical quantification of the Pt shell is particularly important as these Pt−Co particles still show a catalytic advantage over Pt particles, despite the fact that the top three surface layers are pure Pt. Our quantification of the shell thickness following exposure to the oxidizing acidic environment of the cathode suggests that the catalytic enhancement observed in these Pt−Co nanoparticles over pure Pt cannot be due to a nearest-neighbor, or even second-nearest-neighbor electronic effect, as the outermost three atomic layers are pure Pt. Rather, as the Pt shell is coherently strained to the Pt−Co alloyed core, any electronic origin for the boon in catalytic activity is likely to be indirect, such as a change in bandwidth due to a change in lattice constant.[8,28,29,37−39] The shell thickness can grow during electrochemical cycling,[18,23] however with increasing strain energy cost with shell thickness strain enhancement cannot be

sustained for arbitrarily thick Pt shells and must relax beyond some critical thickness.[40]

We now directly study the impact of electrochemical potential cycling by analyzing statistics from spectroscopic images of hundreds of nanocatalysts, before and after cycling. We also measured the electrochemical properties (i.e., hydrogen-adsorption−desorption area, HAD; mass activity, MA; and specific activity, SA) and particle size distributions prior to EELS spectroscopic imaging. The main electrochemical trends (Supporting Information Table S1) are the following: (i) Additional heat-treatment and acid-leaching on the as-received sample produced a drop in HAD and MA. This is perhaps because the manufacturer optimized the treatment of the as-received particles. (ii) Additional heat-treatment and acid-leaching had insignificant influence on particle size distributions. (iii) After 10 000 and 30 000 voltage cycles there were systematic reductions in the HAD, MA, and SA and increased particle growth. Figure 4 shows a collage of EELS spectroscopic images comparing the pre- and postcycled samples. In Figure 4a, the Pt and Co concentration maps show that the precycled, as-received particles have a thin relatively, uniform Pt-rich shell of 7.0 ± 0.2 Å (∼3.2 monolayers) surrounding the Pt−Co core. As expected, the shell in the as-received material is similar in thickness to that of the heat plus acid-treated sample (3.2 ± 0.1 vs 2.6 ± 0.1 monolayers); unsurprisingly the specific activity was similar for these samples. In addition, the Pt-shell thickness appears to be independent of the particle size for the starting material (Figure 5a). We also found that there was no correlation between the particle size and the presence of Ll$_2$ ordering, nor does the ratio of ordered to disordered particles change significantly before and after voltage cycling (1.5 ± 0.5 vs 1.9 ± 0.7, Supporting Information Figure S4).

In comparison to the starting, precycled sample, the voltage-cycled sample has the following distinguishing features: (i) a

nonuniform distribution of Co from multiple Pt−Co cores within many of the particles (e.g., Figure 4c); (ii) much thicker Pt shells for some of the particles (e.g., Figure 4d); (iii) a strong correlation between Pt shell thickness and particle size (Figure 5a); (iv) the particles are more rounded, without clear or well-defined facets (a similar trend can also be seen between the heat treated and acid-leached particles; see Supporting Information Figure S11). For a bimetallic alloy such as Pt−Co, these varied spectroscopic maps provide important clues about the coarsening mechanism(s); without these chemical markers such mechanism would be nontrivial to deduce for pure Pt catalyst nanoparticles.[24] The key is that Co is soluble in acid and will be irreversibly leached from the Pt−Co nanoparticles.[11] In contrast, Pt can reversibly dissolve, redeposit, and reduce via electrochemical processes during operation.[14,19] (As shown in Table 1, nearly eight times as

Table 1. Measured Nanoparticle Core/Shell Radii, Weighted by Particle Volume to Reflect the Change in Co Content before and after Cycling, for the Pt−Co Cores, the Surrounding Pt Shell, and the Entire Particles Comprising Both Pt−Co Core and the Surrounding Pt Shell[a]

	As-received Pt−Co Particles	After 30K cycling	30K Cycled: Multicore	30K Cycled: Single-core
Particle radius (nm)	3.7 ± 0.1	4.5 ± 0.1	5.1 ± 0.16	4.3 ± 0.1
Pt−Co core radius (nm)	3.0 ± 0.2	2.9 ± 0.1	2.8 ± 0.3	2.9 ± 0.2
Pt−shell radius (nm)	0.7 ± 0.2	1.6 ± 0.14	2.3 ± 0.3	1.4 ± 0.2
% of Pt remaining in electrode	95 ± 5	90 ± 5		
% of Co remaining in electrode	89 ± 5	60 ± 5		

[a]Also shown are bulk fractions of Pt and Co present in the electrode (with the remainder in the membrane) determined by electron probe microanalysis before and after voltage cycling. The membrane electrode assembly (MEA) before cycling is listed in the as-received column, although the measurement here is on the actual MEA and not just the powder. Each is normalized separately to the total fraction of that element present in electrode and MEA, that is, after voltage cycling 40% of the Co has migrated out of the electrode and into the membrane.

much Co is lost from the cathode region during the electrochemical cycling as Pt.) Thus, the presence of multiple Pt−Co cores in a single nanoparticle, for example, Figure 4c, suggests that coalescence was a contributing mechanism, while growth of particle size by adding a thick Pt shell that contains no Co, for example, Figure 4d, indicates Ostwald ripening. Continued leaching of Co from the interior of the particles would lead to a significant reduction in the Pt−Co core radius, which was not observed here. Skeletal structures formed by dealloying instabilities can be recognized by the appearance of voids and does not seem to be a major factor for the conditions studied here. In addition, a consequence of viewing thick 3D samples in a 2D projection creates the appearance that that there might be some aggregated particles prior to voltage cycling and that apparent "coalescence" could rather be Pt deposition onto neighboring particles. However, tomography (Supporting Information Figure S5) reveals that these apparent aggregates in the precycling projection image are actually well

separated in 3D. Once the possibility of accidental overlap has been excluded, the presence of multiple Co cores (such as those in Figure 4c) can be used as a signature of coalescence.

A scatter-plot comparison of the Pt-shell thickness, particle size correlation between the pre- and postcycled samples is presented in Figure 5a. Statistical summaries of the main trends are given in Figure 5b−d and Table 1. In sharp contrast to the small, uniform Pt-shells of the precycled sample, by the end of the fuel cell's targeted lifetime, there is a strong dependence of shell thickness on particle size (Figure 5a) with some of the large particles having the largest shell thickness. While the Co core remained essentially unchanged in the surviving particles (3.0 ± 0.2 vs 2.9 ± 0.2 nm, respectively), the most probable radius of the single-core particles increased by 0.6 ± 0.1 nm during cycling, which is entirely attributable to the 0.7 ± 0.3 nm increase in Pt shell thickness (Figure 5d and Table 1) by Pt redeposition. Thus, we can deduce that the thick shells on single core particles, as shown in Figure 4d, are mostly the product of Ostwald ripening rather than continued Co leaching; continued Co leaching would have decreased the size of the Pt−Co core and not produced the observed increase in particle size for the single core particles. Instead much of the Co lost from the cathode (Table 1) seems to have come from the smaller particles that have dissolved away completely. This is again consistent with an Ostwald ripening mechanism where dissolved Pt is more likely to be redeposited on the larger particles, protecting their Co-containing cores, but exposing fresh Co to dissolution on the smaller particles.

As our spectroscopic images allow us to infer which of these mechanisms impacted each particle, we can statistically analyze the Ostwald-ripened particles separately from those that coalesced. In the initial distribution (Figure 4a), we were not able to locate any well-defined, multicore particles in the survey region selected for EELS measurements. In contrast, after voltage cycling, we observe that 48 ± 13% of the larger particles (diameter > 6 nm) have multiple cores (Figure 5b); these multicore particles contribute 19% of the overall surface area (Figure 5c). (Here we plot the surface-area-weighted probability function as the surface is the catalytically active region.) The Pt shells on the coalesced particles grew by 1.6 ± 0.4 nm, double that of growth on the single core particles. Combined with no significant change in the effective Co core radius from coalescence, the most probable particle radius of the coalesced particles grew by 1.4 ± 0.3 nm (Table 1), again twice that of the single-core particles. While particle coalescence, in and of itself, does not mandate a significant rise in shell thickness, nevertheless as shown in Figure 5d, the Pt shells of the multicore particles grew by double that of the single-core particles. The dramatic increase in both particle size and Pt shell thickness for coalesced particles demonstrates an enhanced Pt redeposition compared to single-core particles that have grown by Ostwald ripening alone.

With Co being more soluble than Pt, dealloying of the nanoparticles is another possibility that should be considered. In the simplest model, one might expect that leaching of Co from the surface will leave behind a vacancy-rich Pt shell that, given the diffusion rates for surface migration of Pt or for a vacancy to travel one to two unit cells at room temperature will quickly collapse to a solid Pt shell and slow further diffusion. However, when the etching rate of the Co is comparable to the surface diffusion rate of the Pt, a dealloying instability can set in[41] with local clustering of Pt exposing interior Co, which in turn is leached away leaving a skeletal or "spongy" structure.

Generally, the skeletal structure does not occur for particles smaller than the diffusion length (where Pt is just redistributed on the surface), or below a critical concentration of Co, and critical overpotential (that is a function of the Co concentration).[41] We would not generally expect dealloying for 20−30% Co concentrations at 1 V overpotential, however, some large "spongy" particles (as well as the more typical smaller convex particles) have been reported for similar starting material at a 1.2 V overpotential, based on ADF images.[23] We have found a few large particles with very similar ADF images (Supporting Information Figure S12). They account for roughly 4% of the larger (>10 nm diameter) particles and ∼1% of the total particles after cycling, and a similar fraction of the as-received material, suggesting they were not produced by operation in the fuel cell, nor do they account for a significant fraction of particles. Figure 4e−h (and Supporting Information Figure S12) shows EELS maps from these spongy-appearing particles after voltage cycling. While some pores do exist (Figures 4g,h), most of the dark areas in the ADF image that give the spongy appearance are Pt−Co alloys, while the lighter regions are either pure Pt or Pt-rich Pt−Co alloys. This again illustrates the need for EELS in distinguishing between voids and possible light-element (such as Co or O) enrichment.

Exploiting the improved optics of aberration-corrected STEM to collect the elemental concentration map of an unprecedented number of Pt−Co electrocatalysts at different stages in the fuel cell lifetime allowed us to connect the microscopic surface structure, particle composition and the bulk electrochemical performance with statistical confidence. The method should be useful in the study of most 3D Pt−M catalysts (except perhaps Pt−V where overlap of the V−L with the Pt−N edge may be problematic). In both the starting material and in the acidic environment of the cathode, an ∼3 monolayer Pt shell forms around a Pt−Co core. This shell thickness was independent of terminating facet and notably the preferential segregation of a single monolayer of Pt onto the {111} surfaces of the equilibrium particles did not survive exposure to acid. The well-developed facets of the equilibrium structures also do not survive exposure to acid, with particles taking on more rounded structures. Both these observations may explain why the dramatic enhancement in specific activities reported for {111} over other surfaces for single crystals are so much smaller in nanoparticles.[7,36]

While these acid-leached particles show enhanced catalytic activity over pure Pt, it cannot be due to a nearest, or even second-nearest neighbor, electronic effect of the Co as the three outmost surface layers of the acid-leached Pt−Co particles are Pt. Rather, we find that the shell remains coherently strained to the Pt−Co core, suggesting that the observed boon in specific catalytic activity (compared to pure Pt) could be related to the spacing or arrangement of Pt atoms on the surface, and/or electronic effects such as the change in the d-bandwidth due to a change in the lattice parameter,[28] instead of to a direct electronic coupling to the Co atoms. It is worth noting that despite the solubility of Co, many small Pt−Co cores survive the voltage cycling; this is encouraging for strategies that reduce the Pt loadings required by straining a Pt shell to a non-Pt core.

We also compared the particles before and after voltage cycling to directly address the particle coarsening mechanisms leading to a loss in both catalytic surface area and specific activity; after 0.6−1.0 V cycling, the specific activity of these Pt−Co particles approaches that of pure Pt. Under these operating conditions, we find well-rounded, rather than highly percolated structures. We also find that both Ostwald ripening and coalescence are statistically significant contributors to the reduced surface area/g_{Pt} with approximately half of the larger particles having undergone coalescence. Not only do the coalesced particles have a larger mean particle size than uncoalesced particles, but surprisingly 2.9 ± 0.9 times more Pt (by volume) redeposits on them, likely due to Pt redepositing in a way to minimize the surface curvature of the more complex shape resulting from coalescence. This thick Pt shell formed on the coalesced particles, and some of the others, likely explains the loss of a catalytic advantage over pure Pt. It also demonstrates the complex interplay between the two mechanisms, suggesting that decreasing coalescence (by controlling interactions between support and nanoparticles) would likely also bring a decrease in Pt redeposition and the resulting loss in catalytic activity. The tendency of Pt redeposition to form rounded particles may pose a serious durability challenge for strategies to improve the catalytic activity by engineering the nanoparticle shape, though the structural evolution may differ for particles that start with larger initial faceting or cycle through defined potential ranges.

The ability to record statistically meaningful distributions of microscopic information on inhomogeneous nanoparticles ensembles should prove useful not only for catalysis research, but also for a wider variety of nanoparticle systems where competing processes could be proceeding in parallel.

■ ASSOCIATED CONTENT

Ⓢ Supporting Information

Supplementary methods, video, Tables S1 and S2, and Figures S1−S16. This material is available free of charge via the Internet at http://pubs.acs.org.

■ AUTHOR INFORMATION

Corresponding Author
*E-mail: (D.A.M.) david.a.muller@cornell.edu; (Z.Y.L.) vic.liu@gm.com.

Author Contributions
¶These authors contributed equally to this work.

■ ACKNOWLEDGMENTS

■ REFERENCES

(1) Batson, P. E.; Dellby, N.; Krivanek, O. L. *Nature* **2002**, *418*, 617−620.

(2) Haider, M.; Uhlemann, S.; Schwan, E.; Rose, H.; Kabius, B.; Urban, K. *Nature* **1998**, *392* (6678), 768−769.

(3) Muller, D. A.; Kourkoutis, L. F.; Murfitt, M.; Song, J. H.; Hwang, H. Y.; Silcox, J.; Dellby, N.; Krivanek, O. L. *Science* **2008**, *319* (5866), 1073−1076.

(4) Dresselhaus, M. S.; Thomas, I. L. *Nature* **2001**, *414* (6861), 332−337.

(5) Mathias, M. F.; Makharia, R.; Gasteiger, H. A.; Conley, J. J.; Fuller, T. J.; Gittleman, C. J.; Kocha, S. S.; Miller, D. P.; Mittelsteadt, C. K.; Xie, T.; Yan, S. G.; Yu, P. T. *Electrochem. Soc. Interface* **2005**, *14* (3), 24−35.

(6) Service, R. F. *Science* **2009**, *324* (5932), 1257−1259.

(7) Gasteiger, H. A.; Kocha, S. S.; Sompalli, B.; Wagner, F. T. *Appl. Catal., B* **2005**, *56* (1−2), 9−35.

(8) Mani, P.; Srivastava, R.; Strasser, P. *J. Phys. Chem. C* **2008**, *112* (7), 2770−2778.

(9) Mukerjee, S.; Srinivasan, S. *J. Electroanal. Chem.* **1993**, *357* (1−2), 201−224.

(10) Stamenkovic, V.; Schmidt, T. J.; Ross, P. N.; Markovic, N. M. *J. Phys. Chem. B* **2002**, *106* (46), 11970−11979.

(11) Stamenkovic, V. R.; Mun, B. S.; Arenz, M.; Mayrhofer, K. J. J.; Lucas, C. A.; Wang, G. F.; Ross, P. N.; Markovic, N. M. *Nat. Mater.* **2007**, *6* (3), 241−247.

(12) Toda, T.; Igarashi, H.; Watanabe, M. *J. Electrochem. Soc.* **1998**, *145* (12), 4185−4188.

(13) Greeley, J.; Stephens, I. E. L.; Bondarenko, A. S.; Johansson, T. P.; Hansen, H. A.; Jaramillo, T. F.; Rossmeisl, J.; Chorkendorff, I.; Norskov, J. K. *Nature Chem.* **2009**, *1* (7), 552−556.

(14) Chen, S.; Gasteiger, H. A.; Hayakawa, K.; Tada, T.; Shao-Horn, Y. *J. Electrochem. Soc.* **2010**, *157* (1), A82−A97.

(15) Colon-Mercado, H. R.; Popov, B. N. *J. Power Sources* **2006**, *155* (2), 253−263.

(16) Koh, S.; Toney, M. F.; Strasser, P. *Electrochim. Acta* **2007**, *52* (8), 2765−2774.

(17) Watanabe, M.; Tsurumi, K.; Mizukami, T.; Nakamura, T.; Stonehart, P. *J. Electrochem. Soc.* **1994**, *141* (10), 2659−2668.

(18) Yu, P.; Pemberton, M.; Plasse, P. *J. Power Sources* **2005**, *144* (1), 11−20.

(19) Ferreira, P. J.; la O', G. J.; Shao-Horn, Y.; Morgan, D.; Makharia, R.; Kocha, S.; Gasteiger, H. A. *J. Electrochem. Soc.* **2005**, *152* (11), A2256−A2271.

(20) More, K. L.; Borup, R.; Reeves, K. S. *ECS Trans.* **2006**, *3*, 717−733.

(21) Zhang, J.; Litteer, B. A.; Gu, W.; Liu, H.; Gasteiger, H. A. *J. Electrochem. Soc.* **2007**, *154*, B1006−B1011.

(22) Fuller, T. F.; Gray, G. E. *ECS Trans.* **2006**, *1*, 345−353.

(23) Chen, S.; Sheng, W. C.; Yabuuchi, N.; Ferreira, P. J.; Allard, L. F.; Shao-Horn, Y. *J. Phys. Chem. C* **2009**, *113* (3), 1109−1125.

(24) Shao-Horn, Y.; Sheng, W. C.; Chen, S.; Ferreira, P. J.; Holby, E. F.; Morgan, D. *Top. Catal.* **2007**, *46* (3−4), 285−305.

(25) Lifshitz, I. M.; Slyozov, V. V. *J. Phys. Chem. Solids* **1961**, *19* (1−2), 35−50.

(26) Granqvist, C. G.; Buhrman, R. A. *J. Catal.* **1976**, *42* (3), 477−479.

(27) Wilson, M. S.; Garzon, F. H.; Sickafus, K. E.; Gottesfeld, S. *J. Electrochem. Soc.* **1993**, *140* (10), 2872−2877.

(28) Strasser, P.; Koh, S.; Anniyev, T.; Greeley, J.; More, K.; Yu, C.; Liu, Z.; Kaya, S.; Nordlund, D.; Ogasawara, H.; Toney, M. F.; Nilsson, A. *Nature Chem.* **2010**, *2* (6), 454−460.

(29) Hammer, B.; Norskov, J. K. *Adv. Catal.* **2000**, No. 45, 71−129.

(30) Howie, A. *J. Microsc.* **1979**, *17*, 11−23.

(31) Treacy, M. M. J.; Rice, S. B. *J. Microsc. (Oxford, U.K.)* **1989**, *156*, 211−234.

(32) Crewe, A. V.; Wall, J.; Langmore, J. *Science* **1970**, *168*, 1338−1340.

(33) Voyles, P. M.; Muller, D. A.; Grazul, J. L.; Citrin, P. H.; Gossmann, H.-J. L. *Nature* **2002**, *416*, 826−829.

(34) Krivanek, O. L.; Corbin, G. J.; Dellby, N.; Elston, B. F.; Keyse, R. J.; Murfitt, M. F.; Own, C. S.; Szilagyi, Z. S.; Woodruff, J. W. *Ultramicroscopy* **2007**, *108*, 179.

(35) Shapiro, A. L.; Rooney, P. W.; Tran, M. Q.; Hellman, F.; Ring, K. M.; Kavanagh, K. L.; Rellinghaus, B.; Weller, D. *Phys. Rev. B* **1999**, *60* (18), 12826−12836.

(36) Stamenkovic, V. R.; Fowler, B.; Mun, B. S.; Wang, G. F.; Ross, P. N.; Lucas, C. A.; Markovic, N. M. *Science* **2007**, *315* (5811), 493−497.

(37) Oezaslan, M.; Strasser, P. *J. Power Sources* **2011**, *196* (12), 5240−5249.

(38) Kibler, L. A.; El-Aziz, A. M.; Hoyer, R.; Kolb, D. M. *Angew. Chem., Int. Ed.* **2005**, *44* (14), 2080−2084.

(39) Zhang, J.; Vukmirovic, M. B.; Xu, Y.; Mavrikakis, M.; Adzic, R. R. *Angew. Chem., Int. Ed.* **2005**, *44* (14), 2132−2135.

(40) Matthews, J. W.; Blakeslee, A. E. *J. Cryst. Growth* **1974**, *27*, 118−125.

(41) Erlebacher, J.; Aziz, M. J.; Karma, A.; Dimitrov, N.; Sieradzki, K. *Nature* **2001**, *410* (6827), 450−453.